

# Gravure Printed Ultrathin Layers of Small-Molecule Semiconductors on Glass

Nils Bornemann, Hans Martin Sauer, and Edgar Dörsam<sup>▲</sup>

Institute of Printing Science and Technology, Universität Darmstadt, Magdalenenstraße 2, 64289 Darmstadt, Germany  
E-mail: bornemann@idd.tu-darmstadt.de

**Abstract.** The authors present the feasibility of sheet fed direct gravure printing for ultrathin, organic semiconductor films on ITO coated glass. Printing with chrome plated gravure cylinders is often believed to require flexible substrates to promote fluid transfer to the substrate. However, the results demonstrate a stable process for the small-molecule Spiro-MeOTAD dissolved in toluene on rigid substrates. The authors obtained layer thicknesses in the range of 5–100 nm. They identified certain boundaries for gravure cell size yielding printed films with thickness of 10–15 nm with good homogeneity suitable for organic light emitting diodes or organic photovoltaics. For gravure cells smaller or larger than the optimal range, the printed layer is afflicted with dot- or ribbinglike structures. The authors show that the latter may result from nip-induced Saffman–Taylor instabilities rather than spinodal dewetting or Marangoni effects. Finally, electrical characterization of a completed stack (PEDOT:PSS electrode) give evidence for integrity of the printed semiconductor layers. © 2011 Society for Imaging Science and Technology.  
[DOI: xxxxxx]

## INTRODUCTION

In this article, we present our recent direct gravure printing experiments of ultrathin, small-molecule based semiconductor layers with thicknesses in the range of 5–100 nm on indium tin oxide (ITO) coated glass substrates. Small-molecule semiconductors are well adapted materials for vacuum deposition of layers for organic devices such as organic light emitting diodes (OLEDs) and organic photovoltaics. This manufacturing technique imposes limits to high throughput and cost efficiency. A rapid and reliable solution based coating or printing process can offer many advantages in this respect, as many small-molecule materials are known to be soluble in a variety of solvents. Studies on principal differences between vacuum and solution processed layers and their effect on device performance have been done by Lee et al. using spin-coating techniques.<sup>1</sup> However, spin-coating technique is not suitable for large scale production. It is our aim to close the still persistent gap between spin-coating and laboratory-scale processing methods on one side and to develop a gravure printing process suitable for large volume production of OLED lighting, display, and photovoltaic applications.

Gravure printing is an attractive process addressing both large area and small structured applications of solution processable inks. It is capable of low cost and high throughput production as implemented in the graphics industry since decades. Nevertheless, adapting such a process to the demands of printed (organic) electronic applications is a challenging task and still faces several unresolved issues. Usually, inks for gravure printing have viscosities between 50 and 200 mPa s,<sup>2</sup> whereas small-molecule semiconductors dissolved in organic solvents often exhibit viscosities not above 2 mPa s. Another prominent problem is the stabilization of the printed liquid film after fluid transfer from the gravure cylinder. The gravure cylinder is designed to deposit an array of small fluid droplets on the substrate rather than a homogeneous layer. This feature enables a very precise dosing of the printing fluid. However, the formation of a continuous fluid layer relies on the forces related to the surface tension of the printing fluid and the substrate. This surface leveling process of the liquid printed layer is prone to hydrodynamic instabilities comparable to the Saffman–Taylor instability observed in Hele-Shaw cells.<sup>3</sup> Detailed investigations including calculations on this issue with special focus on the geometries commonly found in large area printing tools have been presented by Voss.<sup>4</sup> Moreover, fluid layers with a thickness of the order of the interaction range of intermolecular binding forces may induce a dewetting problem. The reader will find detailed descriptions of thin film dewetting in the classical review of de Gennes<sup>5</sup> and also in the more recent one by Bonn and Ross.<sup>6</sup> Furthermore, gravure printing on hard and fragile glass substrates with a hard gravure cylinder is delicate for mechanical reasons and a poorly understood process. In graphical printing, it has always been assumed that an intimate mechanical contact between cylinder and substrate along the whole contact line is a precondition of continuous fluid transfer. In contrast, we observe that even for our rigid printing forms and substrates where perfect mechanical contact cannot be achieved even under high mechanical pressure, a nonintermittent fluid transfer is feasible, even throughout a 15 × 15 cm sized substrates. We shall argue that viscous forces in the printing fluid generate a meniscus in the nip, which is able to bridge the inevitably remaining microscopic gaps between gravure cylinder and substrate. The meniscus not only enables fluid transfer on

<sup>▲</sup>IS&T member.

Received Dec. 16, 2010; accepted for publication Apr. 19, 2011; published online Jul. 20, 2011

1062-3701/2011/55(4)/040201/8/\$20.00.

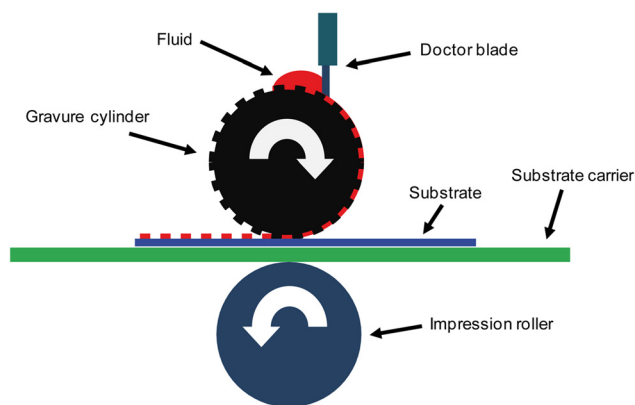


Figure 1. Schematic cross-section of a typical sheet fed gravure printing process.

one hand but also defines the limits of a stable gravure printing process. This implies that the conception of a gravure printing process for organic semiconductor applications should be clearly distinguished from graphical gravure printing.

In principle, one can easily resolve this issue by using flexible polymer substrates. Up to now, however, it has not been possible to provide polymer materials with adequate vapor and oxygen barrier properties. Presently, this feature largely limits the long term stability of organic semiconductors and devices. For OLED devices, it appears plausible that glass will remain the most relevant substrate material for OLED devices within the next years.

This article is organized as follows. In the subsequent paragraphs, we present our gravure printing experiments using dilute solutions of a small-molecule semiconductor (Spiro-MeOTAD). We give an overview of the applied measurement techniques and the device and process parameters which we considered. We analyze the relation between gravure cell size, ribbing instabilities, layer thickness, and surface leveling time. Subsequently, we investigate the origin and the driving forces of the ribbing structure by comparing models of spinodal dewetting and nip-induced Saffman–Taylor type instabilities and develop a qualitative model of printing fluid transfer.

## EXPERIMENTAL SECTION

### Printing Units

Figure 1 shows a schematic cross-section of a typical laboratory-scale, sheet fed gravure printing process. The substrate is guided on a carrier that is accelerated by a driven impression roller on the back of the carrier and the gravure cylinder on top of the substrate. Depending on the type of the tool, the gravure cylinder is driven passively or actively synchronized to the rotation of the impression roller. Ink is predeposited by a doctor blade in order to fill the engraved cells. Mechanical contact of the gravure cylinder and the substrate promotes the ink transfer from cells.

Mechanically engraved gravure cylinders have a chrome plated, chemically inert surface and, hence, are well

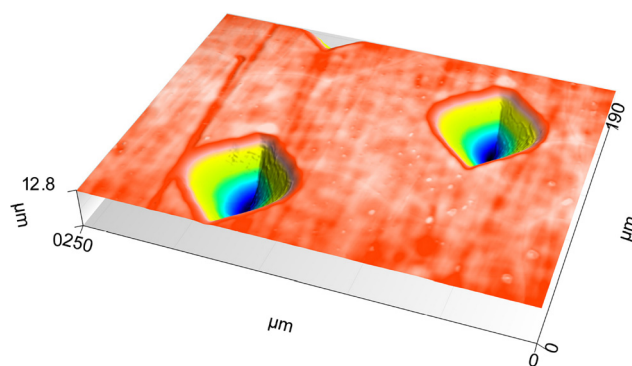


Figure 2. Topography of a mechanically engraved cylinder surface as used in the experiments. Cell depth is  $12.06 \mu\text{m}$  and cell volume  $0.8 \text{ ml/m}^2$ .

suited for many kinds of solvents. Their engravings are usually characterized by cell depth, screen angle, screen frequency (width), and stylus angle. Nonengraved areas have an induced microscaled roughness in printing direction to promote lubrication of the doctor blade and to enhance its lifetime. Figure 2 shows the height profile of the cells mechanically engraved on the cylinder surface as was used in our experiments. Beyond the cells, one finds sander marks on the cylinder surface. These may have impact on ink transport as well and should be considered when discussing gravure printing for electronic applications.

For a detailed description of the gravure printing technique the reader is referred, e.g., to Kipphan.<sup>2</sup> We performed our printing tests using two different gravure laboratory printers handling substrate widths of 50 and 150 mm, respectively. The first tool is an IGT Testing Systems G1 printing proofer and the second one a laboratory printer from Prüfbau. As both printers are usually not designed to handle rigid substrates, we had to adapt two critical design features of the laboratory printers. We modified the substrate transport carrier and guidance in order to avoid bending of the glass substrate under the gravure cylinder. Second, careful adjustment of the printing force distribution along the full width of the gravure cylinder was essential for good results. Since printing experiments on both machines yielded comparable printed semiconductor layers, we restrict further discussion and analysis to the IGT printing proofer.

Our gravure cylinder exhibited eight different fields of  $15 \times 33.5 \text{ mm}$  in size and one of  $30 \times 33.5 \text{ mm}$ . Each field contained a rectangular array of 70 gravure cells per centimeter, each with the shape of an inverted pyramid. The cell depths in the individual fields were different. Their nominal values given by the manufacturer were 11, 14, 17, 20, 24, 26, 28, 30, and  $33 \mu\text{m}$ . Consequently, we shall refer to the fields as F11 to F33, according to their nominal cell depths. The cells had a stylus angle of  $140^\circ$ , and raster lines of the rectangular cell array were rotated by an angle of  $53^\circ$  with respect to the cylinder axis. Before printing, we characterized the cells of the gravure cylinder using a confocal microscope with a high numerical aperture objective

(NA = 0.95). We determined the actual cell depths to be approximately 2  $\mu\text{m}$  less than their respective nominal values. Fig. 2 shows the topography of field F14. In this way, we obtained cell volumes ranging from 0.24 ml/m<sup>2</sup> in F11 to 7.10 ml/m<sup>2</sup> in F33. We should like to emphasize that in graphical gravure printing usually not more than 50% of the cell content is actually transferred to the substrate. We therefore expected average thicknesses of the printed fluid layers on the glass substrate of 120 nm to 3.55  $\mu\text{m}$  in the respective fields. Taking into account the very low concentration of dissolved semiconductor material of 2.5 wt. %, the expected average thicknesses of the dried semiconductor layers were 3 nm for the smallest and 90 nm for the largest cell volume.

### Materials

The glass substrates were provided by Merck KGaA, Darmstadt. The initial size of the edge-polished substrates was 150  $\times$  150 mm. The glass substrates were coated with a sputtered layer of 140 nm ITO. For experiments with the IGT printing proofer, the substrates were cut into stripes of 50  $\times$  150 mm. Two of these stripes were mounted on a substrate carrier plate in a row for each printing run. As the cut edges were not polished, we frequently had to deal with crack formation on the glass substrate during printing. In contrast, the laboratory printer by Prüfbau was able to handle the original 150  $\times$  150 mm ITO glass substrates and provided a very stable and reproducible process, with only extremely rare cases of marginal substrate damage.

In order to remove any residuals from the ITO and to increase the surface tension from 40 mN/m to around 70 mN/m, the substrates were treated with low pressure oxygen plasma (Nano from Diener Electric) before printing. As printing liquid, we used 2.5 wt. % of the small-molecule hole transport semiconductor Spiro-MeOTAD (C<sub>81</sub>H<sub>68</sub>N<sub>4</sub>O<sub>8</sub>, molar weight: 1225.43 g/mol) from BASF SE (Ludwigshafen, Germany) dissolved in toluene. We determined its viscosity to be  $\eta = 0.72$  mPa s and its surface tension to be  $\sigma = 27.6 \pm 0.3$  mN/m. Surface tension remains more or less constant as solute concentration is raising. Eventually, a minimal increase is to be expected, as depicted in Figure 3. The maximum solubility at room temperature is around 8.5 wt. %.

### Sample Analysis

Measurements of surface tension of liquids and substrates were carried out with a drop shape analysis tool DSA100 from Krüss, and viscosities were determined with a Haake Mars III. The drying process of the liquid film was recorded immediately after each printing run using a digital camera (Canon EOS 5D Mark II). In this way, we were able to identify the evolution of local thickness in-homogeneities and to determine drying times of the semiconductor solution in the individual fields. The dry layers were subsequently examined using optical microscopy (Leica DM4000). Layer thickness and surface topography were obtained with an optical profiler Sensofar PLu Neox using

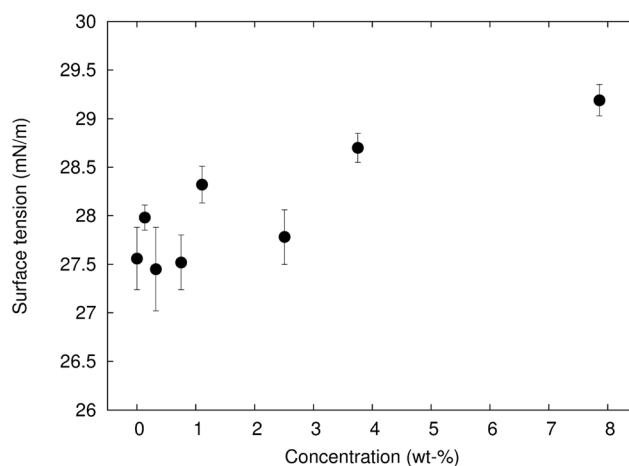


Figure 3. Surface tension vs concentration of the small-molecule Spiro-MeOTAD dissolved in toluene.

white light and phase shift interferometry. On some of the substrates, lateral thickness undulations were examined with an atomic force microscope (Nanosurf LensAFM). The confocal mode of the PLu Neox was used to characterize the gravure cylinders as described above. In order to verify the electrical integrity of the printed semiconductor layers, a Schottky diode stack was completed applying an inkjet printed electrode of PEDOT:PSS (Clevios by H. C. Stark) with a Dimatrix printer. Current–voltage characteristics were recorded with a computer controlled source measure unit (SMU) Keithley 2400.

### Printing and Drying

Immediately after the moment when the processed glass substrate had left the laboratory printer, we observed that transfer of printing fluid was successful in all fields of each sample. Closed liquid films were formed on the glass substrate, with transfer volumes related to the individual fields of the gravure cylinder in the expected range. Within the next few seconds, specific reproducible pattern formation was observed in the liquid film. Figures 4(a) and 4(b) show multistep microscope images of a typical sample of two consecutively printed glass pieces with printing speed of  $v_p = 1$  m/s and printing pressure of  $p_p = 8$  N/cm of cylinder width. The rectangular pattern strongly visible in fields F11 and F14 is an artifact, which originates from the stitching procedure of the microscope images.

In contrast to the fields F11–F24 with small transfer volumes, the fields F26–F33 with larger transfer volumes exhibit large scale thickness undulations and diffuse borders. Printing results were not well reproducible here. Field F24 shows striplike patterns in printing direction. In the fields F17 and F20 of Fig. 4(b), plots of the Fourier transformations (FFT) of the patterns are inserted, showing the predominant wavenumbers, the corresponding wavelengths, and the lateral isotropy of the patterns. Radial averaging of the FFT plots reveals reproducible wavelengths of  $\lambda_{F17} = 0.73$  mm for field F17 and  $\lambda_{F20} = 1.17$  mm for F20.

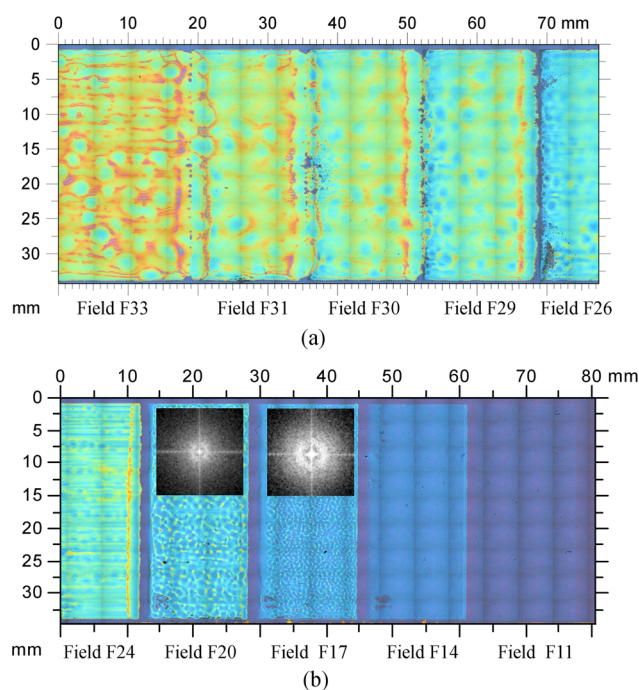


**Figure 4.** Multistep bright field microscope images of a dry printing result on two consecutively fixed glass substrates of  $50 \times 150$  mm, printing direction is to the left. Printing speed was  $v_p = 1$  m/s and printing pressure  $p_p = 8$  N/cm. Substrate (a) was printed prior substrate (b). Field F17 and F20 have insets of two-dimensional FFTs yielding wavelength of  $\lambda_{F17} = 0.73$  mm and  $\lambda_{F20} = 1.17$  mm.

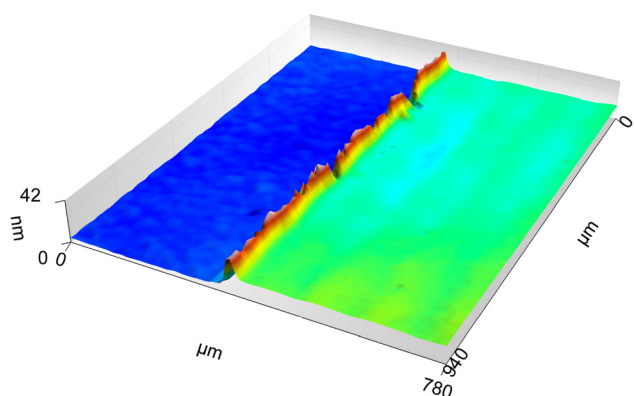


**Figure 5.** Topography determined with phase shift interferometry at a border of a printed field F14 (ITO surface on the left, Spiro-MeOTAD layer on the right). The roughness (rms) of the film without the ridge is  $0.853$  nm.

The film thicknesses were analyzed with phase shift interferometry at the borders of each field. Figure 5 shows a typical topography of the printed field F14, and Figure 6 displays the average step height perpendicular to the rim. The topography of the field F17 in Figure 7 depicts the undulations that are also visible in the microscope images in Fig. 4(b). The printed fields always exhibit a ridge at the borders.

In this way, we obtained average layer thicknesses of the fields F14, F17, and F20. The topography measurements of field F14 show a very reproducible homogeneous layer of  $10$  nm with very small undulations of the gravure cell period (screen width), namely  $\lambda_{F14} = 0.143$  mm. On the contrary, in field F11, the printing fluid droplets deposited by

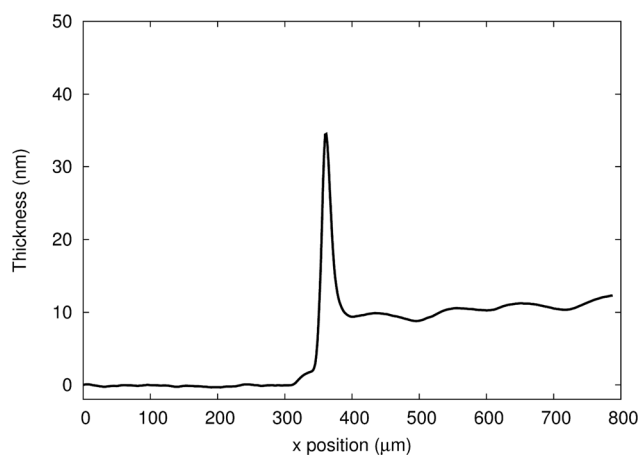


**Figure 6.** Averaged profile of the topography of field F14 shown in Fig. 5. The ridge has an average height of  $34.8$  nm and the layer of  $10.5$  nm.

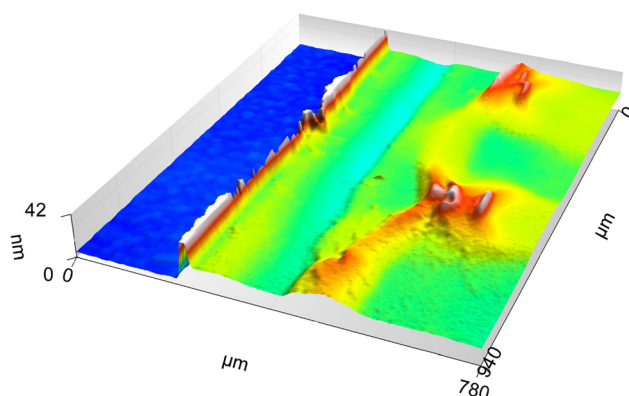


**Figure 7.** Topography determined with phase shift interferometry at a border of a printed field F17 (ITO surface on the left, Spiro-MeOTAD layer on the right). To visualize the layer, the ridge height is cut at  $42$  nm (maximum ridge height is  $97$  nm). The surface undulations are clearly visible. The roughness (rms) of the film without the ridge is  $4.33$  nm.

the individual cells of the gravure cylinder did not spread on the substrate toward neighbored droplets. Rather, they formed well-separated, cake-shaped circular spots with a diameter of around  $120$   $\mu\text{m}$  and an average height of  $8$  nm as shown in Figure 8. The small spots at the top of the image are deposited semiconductor material that may originate from fluid transfer from sand marks of nonengraved areas.

Taking into account the concentration of  $2.5$  wt. % of the solute, we conclude that approximately  $44\%$  of the fluid contained in the cells was actually transferred to the substrate in field F11. In a similar way, we reconstructed wet film thicknesses and transfer ratios of other fields, as summarized in Table I. We determined also the time spans from the fluid transfer to the moment when each printed field completed the drying phase, see Table I.

In order to check whether the printed films would be adequate for device fabrication, we completed the layer stack in the fields F14 and F17 by a contact layer of PEDOT:PSS, which we applied with a Dimatrix ink jet printer. We applied a set of five contact pads of approximately  $2 \times 2$  mm in size on each of the two fields. After thorough drying of the

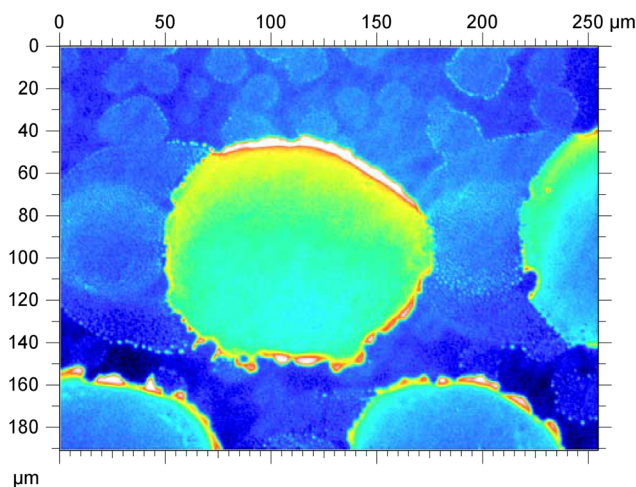


Figure 8. Image of printed field F11 determined with phase shift interferometry. The big spots represent the fluid transfer of corresponding gravure cells; the average height is 8 nm.

Table I. Parameters determined for printed fields F14–F20.

Field	F14	F17	F20
Dry film thickness $h_d$ (nm)	10.5	14.98	19.98
Wet film thickness $h$ ( $\mu\text{m}$ )	0.39	0.6	0.8
Dominant wavelength $\lambda_f$ (mm)	0.143	0.73	1.17
Drying time $\tau_d$ (s)	0.76	1.84	3.08
Transfer ratio	0.50	0.43	0.35

PEDOT:PSS ink, we recorded the current characteristics of these Schottky diodes using a Keithley 2400 SMU. The plots (see Figure 9) clearly show a typical diode characteristic. As expected, the diode performance is slightly superior for the 10 nm layer as compared to the 15 nm layer. This demonstrates the electrical integrity of the printed layers in spite of their very small thicknesses of only 10 nm with respect to 15 nm. It also excludes the presence of short circuits due to layer pinholes or defects with sizes below 100 nm, which we would not have been able to detect in our optical surface profiles.

## THEORY AND DISCUSSION

Our experiments identify a range of printing parameters where reproducible generation of ultrathin, continuous semiconductor layers free of electrical defects is feasible by gravure printing. It is quite surprising that this stable regime corresponds to layer thicknesses between 10 and 20 nm, with printing fluid transfers of 0.4 to 0.8 ml/m<sup>2</sup>. Also, the viscosity of the printing fluid is more than 1 order of magnitude smaller than viscosities of gravure printing inks commonly used in graphical printing and is comparable to ink jet printing inks. The stable regime is limited toward smaller transfer quantities, as in field F11, by the fact that film drying time decreases with film thickness and that consequently surface undulation in the liquid film cannot be leveled by the surface tension any

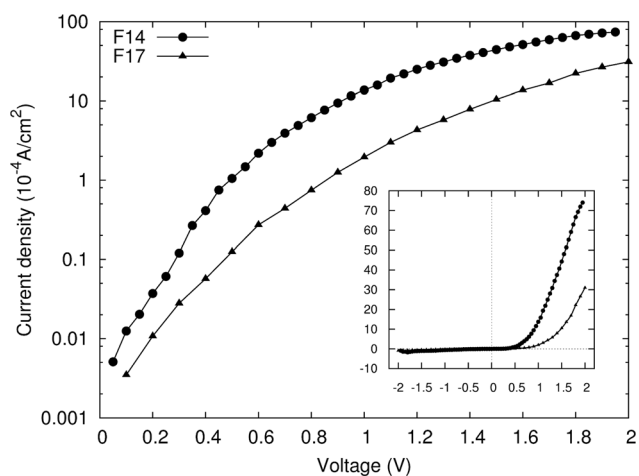


Figure 9. Current density–voltage characteristics of a stack of ITO, gravure printed Spiro-MeOTAD and inkjet printed PEDOT:PSS of fields F14 and F17. The inset shows the linear plots for the current density and voltage.

longer. For higher transfer quantities, as in the fields F20 and larger, surface undulations at wavelengths considerably larger than the gravure cell distance emerge and become more and more pronounced. These undulations are highly undesired in functional printing. However, in the present case, they offer some insight why gravure printing is possible using hard printing forms and hard substrates. The existence of such thickness undulations, e.g., in flexographic printing, has long been known, and is quite analogous to the Saffman–Taylor instability of a Hele-Shaw cell.<sup>3</sup> The instability occurs at the instant when the printing form is lifted off the substrate, and it has been discussed with respect to large area printing techniques by Voss.<sup>4</sup> We also refer to the work of Gaskell et al. who consider similar phenomena in roll-coating machines.<sup>7</sup> Here it is shown that the emerging thickness undulations have a predominant wavelength, which scale with the thickness  $h$  of the fluid film as follows:

$$\lambda_{\text{ST}} = \sqrt{\frac{\eta v_p h^3}{\sigma X}}, \quad (1)$$

where  $\eta$  is the viscosity of the printing fluid,  $\sigma$  the surface tension,  $v_p$  the printing velocity, and  $X$  the distance of the fluid meniscus at the nip to the point where the gravure cylinder touches the glass substrate. In many cases, but not always, the thickness patterns are oriented in printing direction. Due to surface tension, the created patterns level on a characteristic time scale, which essentially depends on the wavelength  $\lambda$  and the film thickness  $h$  according to:<sup>8</sup>

$$\tau_{\text{lev}}(\lambda, h) = \frac{3\eta\lambda^4}{16\pi^4\sigma h^3}. \quad (2)$$

If a Saffman–Taylor type instability is effective at the moment of fluid transfer, the resulting patterns should exhibit structures with typical length scale  $\lambda_{\text{ST}}$  and disappear

after a leveling time of the order of  $\tau_{lev} (\lambda_{ST} h)$ . The patterns will not survive on the dried film unless drying time  $\tau_d$  is smaller than or of the order of the leveling time  $\tau_{lev}$ .

As an alternative explanation, we consider the case where a disjoining pressure is present in the printed liquid films. The disjoining pressure emerges when the film thickness is of the order of the interaction range of the intermolecular forces, i.e., Van der Waals forces. Therefore, it critically depends on the local film thickness. Local gradients in disjoining pressure give rise to a fluid flow from thinner to thicker regions of the fluid film and may even result in a local dewetting on the substrate. Different from the effect of nip instability, the disjoining pressure promotes pattern formation in the time span between printing and drying. Here, it is assumed that, after ink transfer from the gravure cylinder to the substrate, the liquid forms a more or less uniform film on the substrate. With ongoing evaporation of the solvent, the film thickness becomes finally comparable to the interaction range of intermolecular Van der Waals forces, which are of order of few 10 s of nm.<sup>9</sup> The disjoining pressure then drops drastically as the liquid layer thickness is further decreasing:

$$p_{disj}(h) = -\frac{A}{12\pi h^2}, \quad (3)$$

with  $A$  as the Hamaker constant of the solvent. The reader is referred to the excellent reviews of de Gennes,<sup>5</sup> Craster and Matar,<sup>10</sup> and Bonn et al.<sup>11</sup> on this phenomenon. In the lubrication approximation of the Navier–Stokes equations for thin films, the disjoining pressure may give rise to a spinodal dewetting process on the substrate. At the onset of this, process thickness modulations of typical pattern sizes of

$$\lambda_s = \sqrt{-\frac{8\pi^2\sigma}{\partial^2 p_{disj}/\partial h^2}} \quad (4)$$

will emerge.<sup>12–15</sup> The time scale on which such patterns evolve is given by

$$\tau_s = 48\pi^2\eta\sigma \frac{h^5}{A^2}. \quad (5)$$

In analogy to the Saffman–Taylor instability, the pattern formation time should be related to the drying time  $\tau_d$ . Spinodal dewetting may cause patterns of the observed kinds if the time scale  $\tau_s$  is smaller than or at least of the order of the drying time scale. Otherwise, the liquid film will be leveled by surface tension and form a more or less homogeneous layer as described above.

We have plotted corresponding time scales and pattern sizes, which may be due to the two described instability mechanisms in Figures 10 and 11 for given material parameters. For the graphs of Eqs. (4) and (5) in Fig. 11, the Hamaker constant was estimated via Lifshitz theory using refractive indexes of  $n_{ITO}=2$  and  $n_{toluene}=1.497$  and

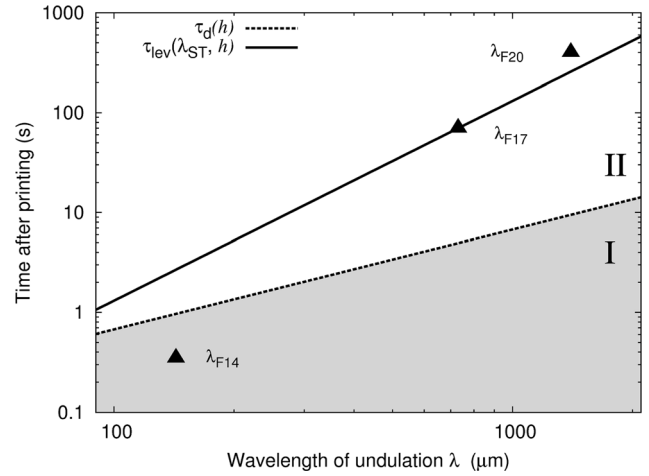


Figure 10. Leveling time and Saffman–Taylor instability. The plots show the leveling time  $\tau_{lev}$  for  $\eta=0.72$  mPa s and  $\sigma=27.56$  mN/m. The triangles represent the observed undulations  $\lambda_{F14}$ ,  $\lambda_{F17}$ ,  $\lambda_{F20}$  according to the leveling time of their wet film thicknesses (see Table I). The drying time  $\tau_d$  was extrapolated using the estimated drying times of fields F14–F20.

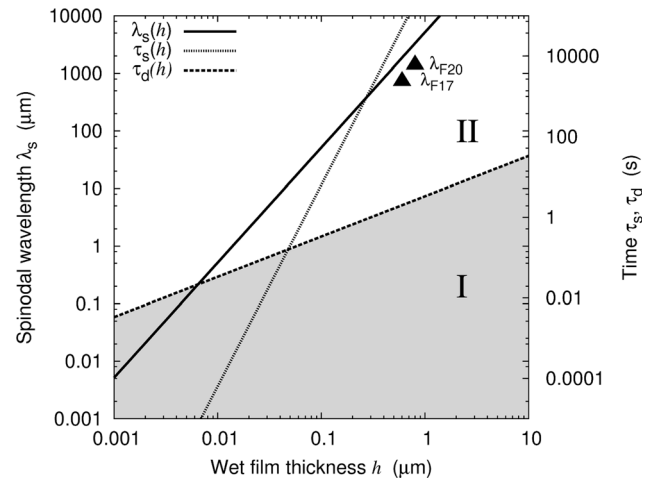


Figure 11. Spinodal dewetting. Spinodal wavelength  $\lambda_s$  and rupture time  $\tau_s$  for system parameters  $\eta=0.72$  mPa s,  $\sigma=27.56$  mN/m, and the Hamaker constant  $A=1.2165 \cdot 10^{-20}$  J for ITO–toluene interface. The drying time  $\tau_d$  was extrapolated using the estimated drying times of fields F14–F20.

dielectric constants of  $\epsilon_{ITO}=9.0$  and  $\epsilon_{toluene}=2.379$ .<sup>9</sup> For the discussion of the model, here we neglected evaporation, diffusion, short-range forces, and polar interactions of substrate and fluid that might rescale the dependencies. In both figures, we have extrapolated the drying time  $\tau_d$  as estimated from the videos recorded from the drying process. They separate the plots tentatively into two regions indicating that drying suppresses corresponding dynamics (region II) or allows them to evolve (region I). In Fig. 11, the triangles represent the undulations determined in the fields F14, F17, and F20 corresponding to wet film thicknesses  $h=0.4$   $\mu\text{m}$ ,  $h=0.6$   $\mu\text{m}$ , and  $h=0.8$   $\mu\text{m}$  (see Table I). The undulation of F14 can be clearly identified with the screen width of 143  $\mu\text{m}$  (70 l/cm). The leveling time for this period is in the region of the drying time and

therefore in good agreement with the small residual amplitude of 2 nm observed here. In Fig. 10, we have also included an extrapolated curve for the leveling time  $\tau_{lev}$  ( $\lambda_{ST}$ ,  $h$ ) related to the Saffman–Taylor wavelength  $\lambda_{ST}$  according to Eq. (1). The scaling of the predominant wavelengths above 0.73 mm (field F17) with liquid film thicknesses above 0.6  $\mu\text{m}$  (triangles  $\lambda_{F17}$  and  $\lambda_{F20}$  in Fig. 10) is in reasonable agreement with the Saffman–Taylor model. Moreover, the times required for drying are short enough to explain why surface leveling of the liquid films could not be completed for these wavelengths (corresponding times of wet film thicknesses of  $\lambda_{F17}$  and  $\lambda_{F20}$  can be found in the region II of Fig. 10). This point of view is supported by the observation that the patterns are partly oriented in printing direction (field F24 and above) and the good qualitative agreement of predicted and observed pattern sizes. However, there is a lack of understanding why the pattern orientations in the fields F17 and F20 are apparently uncorrelated with printing direction. This point clearly requires further research.

As an additional sign toward the Saffman–Taylor instability, one finds a thickened edge in the fields F14 to F33 at the borders situated forward with respect to the printing direction. This indicates that the printing fluid is no longer deposited here in isolated droplets but is forming a continuous meniscus, which extends over the walls of the gravure cells. This meniscus accumulates an excess of printing fluid. When the last row of the gravure cells within the specific field is lifted from the substrate, this excess volume is abandoned to the substrate and squeezed by the nonengraved surface parts of the gravure cylinder. After drying, this results in a seam at the respective border of the field. The excess of printing fluid in the nip is the reason why the walls between the gravure cells are merged in printing fluid when passing the nip. Hence, the conditions for a Saffman–Taylor instability to occur are satisfied. This also explains how the printing fluid may be transferred from the gravure cylinder to the substrate even if there is no direct mechanical contact. As the excess of printing fluid fills possible small gaps between cylinder and substrate, a hydrodynamical contact of the fluid in the cells to the substrate is provided.

We also consider spinodal dewetting as a possible mechanism for the observed patterns in the fields F17 and F20 for two reasons. We are dealing with film thicknesses notably below 100 nm where intermolecular forces can be dominant, and spinodal dewetting has at its onset an isotropic character. According to Eq. (5), we find good agreement for the characteristic wavelength of the fields F17 and F20 (triangles of Fig. 11), whereas related spinodal rupture times are of the order of  $10^4$  s and far beyond the drying times (region II of Fig. 11). Rather, the observed drying times of only few seconds would imply spinodal wavelengths of the order of 1–10  $\mu\text{m}$  to evolve (region I of Fig. 11). Atomic force measurements on this length scale have shown that no such patterns exist in the film. We should emphasize here that the models presented above do not take gradients in surface tension, viscosity, diffusion, and concentration into account; these can

drastically influence the dynamics and might explain the observations in more detail.

As a further origin of the observed surface patterns in the fields with larger transfer volume, we also considered Marangoni-type instabilities or a coffee ring effect. These instabilities are related to an increase of surface tension in the printing fluid with increasing solute concentration and are known to occur for numerous solvent–solute combinations. In thin liquid films, this effect gives rise to a fluid drag from regions with lower solute concentrations toward regions with higher concentration. In a final state of film drying, one obtains characteristic wall patterns of deposited solute at the borders of the printed film, as depicted in Figs. 5–7. One could imagine that such effect, if present, could be responsible for the patterns observed here as well. However, our measurements of the surface tension of the printing fluid using different solute concentrations (Fig. 3) show that there is no significant increase of surface tension with increasing concentration of our solute. Moreover, even if the Marangoni effect were relevant, it could amplify the observed thickness undulations, but it could not explain how the fluid film selects the predominant wavelength of the patterns.

Summarizing these results, we cannot definitely assign the observed patterns for the fields F17 and F20 to one of the two instability mechanisms discussed here, whereas it is quite obvious that Saffman–Taylor instabilities are responsible for the patterns in the fields F24 to F33. This also could explain how ink transfer between the hard gravure cylinder and the glass substrate is accomplished in spite of the fact that direct mechanical contact cannot be achieved at every point. The occurrence of a Saffman–Taylor instability along the nip implies a continuous fluid meniscus over the complete width of the substrate. Quite different from the classical understanding of the gravure printing process, the printing fluid is not only deposited from the gravure cells of the cylinder. Due to its very low viscosity and the presence of an excess of volume, the printing fluids also wets the walls between the gravure cells, which supports the formation of a continuous meniscus and, hence, the Saffman–Taylor instability. As cell volumes are further reduced while cell distances remain constant, we obtain a transition from the continuous meniscus to single cell transfer (fields F20–F11). In this process, a specific combination of fluid volume, drop distance, spreading, and leveling time lead to the formation of a flat, homogeneous layer (in our experiments, field F14). It remains unresolved whether field F14 was produced with a continuous meniscus or separated drops. This would require a closer understanding of the isotropic pattern formation of the fields F17 and F20.

## CONCLUSIONS

In this article, we have reported studies on the critical parameters of direct gravure printing of high quality, nanometer thick small-molecule semiconductor layers on ITO glass substrates. We have found that transfer of the low viscosity printing fluid as would also be processable with ink jet printers was feasible in a quite large range of 5–100 nm, but

that the printed layers are subject to hydrodynamical instabilities, namely the Saffman–Taylor instability and possibly spinodal dewetting phenomena, which give rise to an inhomogeneous film thickness. These effects may therefore spoil performance and homogeneity of organic semiconductor devices such as light emission of printed OLED panels.

An adequate and stable process window for producing semiconductor layers of 10–20 nm in thickness has been identified by adapting the cell volume of the gravure cylinder in order to avoid Saffman–Taylor-like instabilities on one hand and transfer of isolated fluid droplets on the other hand. The effects governing the development of thin layers are closely related to microscopic dewetting phenomena. Moreover, Marangoni-type liquid film instabilities might be relevant as well in general, although it is not plausible that they could be responsible for the emergence of a predominant structure size in our patterns. Our experiments also question the typical understanding of fluid transfer in gravure printing and the applicability of standard gravure cylinders for high quality functional printing.

#### ACKNOWLEDGMENTS

The authors are grateful to Ingo Münster, BASF SE Ludwigshafen, and Klaus Bonrad, Merck KgaA Darmstadt, and their research groups for the support of our work and for the generous donation of OLED printing liquids and substrate materials. The authors appreciate the support by the InnovationLab GmbH, Heidelberg. Moreover, this work has been funded by the Bundesministerium für Bildung und Forschung, Germany, under Grant No. 13N10760 (PrintOLED).

#### REFERENCES

- <sup>1</sup> T.-W. Lee, T. Noh, H.-W. Shin, O. Kwon, J.-J. Park, B.-K. Choi, M.-S. Kim, D. W. Shin, and Y.-R. Kim, “Characteristics of solution-processed small-molecule organic films and light-emitting diodes compared with their vacuum-deposited counterparts”, *Adv. Funct. Mater.* **19**, 1625–1630 (2009).
- <sup>2</sup> H. Kippphan, *Handbook of Print Media: Technologies and Production Methods* (Springer, Berlin, 2001).
- <sup>3</sup> P. G. Saffman and G. Taylor, “The penetration of a fluid into a porous medium or Hele-Shaw cell containing a more viscous liquid”, *Proc. R. Soc. A: Math. Phys. Eng. Sci.* **245**, 312–329 (1958).
- <sup>4</sup> C. Voss, “Analytische Modellierung, Experimentelle Untersuchungen und dreidimensionale Gitter-Boltzmann-Simulation der quasistatischen und instabilen Farbspaltung”, Ph.D. thesis (University of Wuppertal, Wuppertal, Germany, 2002).
- <sup>5</sup> P. de Gennes, “Wetting: Statics and dynamics”, *Rev. Mod. Phys.* **57**, 827–863 (1985).
- <sup>6</sup> D. Bonn and D. Ross, “Wetting transitions”, *Rep. Prog. Phys.* **64**, 1085 (2001).
- <sup>7</sup> P. H. Gaskell, G. E. Innes, and M. D. Savage, “An experimental investigation of meniscus roll coating”, *J. Fluid Mech.* **355**, 17–44 (1998).
- <sup>8</sup> N. Bornemann, H. M. Sauer, and E. Dörsam, “Thin film behaviour after ink transfer in printing processes”, *Proc. of LOPE-C (OE-A, Frankfurt, Germany, 2010)*, p. 138, ISBN: 978-3-00-029955-1.
- <sup>9</sup> J. Israelachvili, *Intermolecular and Surface Forces*, 2nd ed. (Academic, London, 1991).
- <sup>10</sup> R. Craster and O. Matar, “Dynamics and stability of thin liquid films”, *Rev. Mod. Phys.* **81**, 1131–1198 (2009).
- <sup>11</sup> D. Bonn, J. Eggers, J. Indekeu, J. Meunier, and E. Rolley, “Wetting and spreading”, *Rev. Mod. Phys.* **81**, 739–805 (2009).
- <sup>12</sup> L. Landau and B. Levich, “Dragging of a liquid by a moving plate”, *Acta Physicochim. URSS.* **42–54** (1942).
- <sup>13</sup> A. Vrij, “Possible mechanism for the spontaneous rupture of thin, free liquid films”, *Discuss. Faraday Soc.* **42**, 23 (1966).
- <sup>14</sup> U. Thiele, M. Mertig, and W. Pompe, “Dewetting of an evaporating thin liquid film: Heterogeneous nucleation and surface instability”, *Phys. Rev. Lett.* **80**, 2869–2872 (1998).
- <sup>15</sup> O. Bäümchen and K. Jacobs, “Slip effects in polymer thin films”, *J. Phys.: Condens. Matter* **22**, 033102 (2010).